J. Plasma Physics (1997), *vol.* 58, *part* 4, *pp.* 747–769. Printed in the United Kingdom
© 1997 Cambridge University Press

Parametric instabilities of trapped upper-hybrid oscillations

E. MJØLHUS

Institute of Mathematical and Physical Sciences, University of Tromsø, N-9037 Tromsø, Norway

(Received 30 april 1997)

Parametric instabilities of upper-hybrid oscillations trapped in a plasma density depletion across an ambient magnetic field are investigated. Approximate dispersion relations are derived, which lead to the identification of two parametric instabilities of the localized upper-hybrid bounded wave structure. Both are related to trapped upper-hybrid oscillation resonances. The first is a decay to a frequency of a trapped wave resonance, downshifted from the applied frequency, where the downshift must be slightly larger than the lower-hybrid frequency. The second instability can exist when the applied frequency is slightly below the arithmetic mean of the frequencies of two trapped oscillation resonances; then the antiStokes component of one is in resonance with the Stokes component of the other. Both slab and two-dimensional geometries are considered.

1. Introduction

The investigation to be described in this paper was motivated by observations in experiments where a powerful (O-mode) HF wave was transmitted from ground into the ionosphere. When the return wave was frequency-analysed, interesting sideband structures were detected; they have been termed SEE (stimulated electromagnetic emissions). The first report of this phenomenon was in Thidé *et al.* (1982), and they have since been extensively investigated. Another phenomenon observed in such radio experiments, is striations, i.e. plasma density irregularities induced by the HF exposure, with a small scale across the magnetic field and very elongated along the magnetic field (Fialer 1974; Minkoff *et al.* 1974). Recent SEE experiments (Leyser *et al.* 1989, 1994; Stubbe *et al.* 1994; Waldenvik 1994) strongly indicate that the two phenomena described above are related. In order to obtain a theoretical model for the generation of the SEE sidebands, one is therefore led to a study of upper-hybrid oscillations driven by the oscillating electric field of the incident radio (pump) wave, and trapped in the density depletions of the striations.

This picture lies at the basis of theoretical models of the process leading to the formation of the striations themselves (Dysthe *et al.* 1982; Inhester 1982; Mjølhus 1983; Gurevich *et al.* 1995). However, in these works the density depletion trapping and generating the upper-hybrid oscillations was treated as pre-existing, assumed to have been formed by slow thermal processes, while the self-consistent ponderomotive density modification was neglected. In order to obtain generation of electromagnetic sidebands in connection with the striations, ponderomotive effects must

https://doi.org/10.1017/S0022377897005886 Published online by Cambridge University Press

be included. This was recently done by Mjølhus and Helmersen (1997), who discovered numerically that parametric instabilities of these trapped upper-hybrid oscillations played a crucial role in explaining the SEE.

The objective of the present paper is to describe a theoretical derivation of these parametric instabilities. The theoretical model will consist of an equation for the upper-hybrid electric field structure as a response to the density perturbation and the pump electric field, and an equation for the lower-hybrid density response to the ponderomotive pressure of the high-frequency electric field. However, the total density perturbation will, in addition to the ponderomotive response, also contain a prescribed part, describing the striation formed by slow thermal processes not included in the dynamical model.

It will be argued that, at least for sufficiently small pump fields, this model allows a stationary solution. The dependence of this stationary solution on the parameters of the model will play a crucial role in the theory. As was discussed in Mjølhus (1983) and Dysthe *et al.* (1982), there are resonant cases, where an undriven, undamped standing wave can exist in the density depletion; then the amplitude in the driven, weakly damped case will be large. These parameter values will be called trapped upper-hybrid resonances. The parametric instabilities that will be identified in this paper can be described in terms of these resonances. In the first, the trapped oscillations decay (TOD) instability, the growing mode is at the frequency of a trapped upper-hybrid resonance; at the same time, this frequency is downshifted from the applied frequency slightly more than the lower-hybrid frequency. Linearizing around the stationary trapped upper-hybrid oscillations, a simplified approximate dispersion relation will be obtained, allowing this interpretation. In contrast to standard accounts (e.g. Mannheimer and Ott 1974) of parametric instabilities for a uniform medium, or in a slowly varying medium (Rosenbluth 1972), no wavenumber matching condition enters the description of this instability, although such conditions can be identified in a WKB limit.

The second instability, which is termed the Stokes–antiStokes (S–aS) instability, may be seen as a counterpart of the oscillating two-stream instabililty (Sanmartin 1970) in the present context: when the applied frequency is (slightly below) the mean value of the frequencies of two trapped upper-hybrid resonances, the Stokes component of one will be in resonance with the antiStokes component of the other. This situation will be shown to lead to an instability. The S–aS instability usually has higher threshold than the TOD; however, there are parameter regions where only the S–aS instability can exist.

The mathematical approach can be characterized as a Galerkin method. Results are expressed in terms of integrals involving eigenfunctions and trapped oscillation field structures, although explicit expressions for these cannot be given. Thus the treatment has a global character, and no special assumptions on, for example, the density profile are made. Although the present treatment is rather specific, it is thought that the general method is also applicable to other, similar, situations. The essential properties appear to be that one participating mode (the upper-hybrid) is sensitive to the background plasma state and thus subject to trapping and resonances, while the other (the lower-hybrid) is not affected by the local changes of plasma state, and consequently is not subject to trapping and resonances.

The plan of the paper is as follows. In Sec. 2, the basic model is stated. In Sec. 3, the question of stationary solutions is posed, and the resonance structure is discussed. In Sec. 4, the linearization is introduced, and a general (though approxi-

https://doi.org/10.1017/S0022377897005886 Published online by Cambridge University Press

mate) dispersion relation is obtained. In Sec. 5, a further approximation leads to the trapped oscillations decay instability, while in Sec. 6 the Stokes–antiStokes instability is discussed. For simplicity, all this will be done for slab geometry. In Sec. 7, it is demonstrated how the theory can be extended to the situation of two-dimensional striations varying perpendicularly to the magnetic field. In Sec. 8, a brief discussion is given of the application of the present processes to the problem of SEE generation, and in Sec. 9, some summarizing comments are given. The theory is supported with numerical examples; in Appendix A, some comments on the numerical model are given. In Appendix B, some mathematical details are collected.

2. Basic equations

Assume a magnetized plasma with a (quasineutral) density variation of the form

$$n_{\rm tot}(x,t) = n_0 + N(x) + n(x,t). \tag{1}$$

Here n_0 is the background density, to be assumed spatially and temporally constant, $N(x)$ is a localized density depletion assumed to have been brought about by, for example, slow heating and transport processes not accounted for in the present model; x is a coordinate across the ambient magnetic field (assuming slab geometry), and $n(x,t)$ is a further self-consistent perturbation of the density. The state consisting of the two first terms of (1) is exposed to an oscillating long- (i.e. infinite-) wavelength electric field of frequency ω_0 being near, though slightly smaller than the upper-hybrid frequency of the background state n_0; thus we assume an electric field of the form

$$\mathbf{E} = \tfrac{1}{2}\left\{[\mathbf{E}_0 + E(x,t)\mathbf{e}_x]\exp(-i\omega_0 t) + \text{c.c.}\right\}, \tag{2}$$

where $E(x,t)$ is a self-consistent electrostatic response. For this situation, we shall consider the equations

$$\{i(\partial_t + \nu) + [\mathbf{\Omega} - (n+N) + \partial_x^2]\}E = E_0(n+N), \tag{3a}$$

$$(\partial_t^2 - \partial_x^2 + \mathbf{\Omega}_{LH}^2)\, n = \partial_x^2 |E + E_0|^2 \tag{3b}$$

as an appropriate dynamical model. The units in this set of equations are X (space), T (time), $\tilde{N}$ (particle density) and $\tilde{E}$ (electric field) given by

$$X = \frac{3}{2}\left(\frac{M}{m\eta}\right)^{1/2}\lambda_D, \tag{4a}$$

$$T = \frac{3}{2\eta}\,\frac{M}{m}\,\frac{1}{\omega_0}, \tag{4b}$$

$$\tilde{N} = \frac{4\eta}{3}\,\frac{m}{M}\,n_0, \tag{4c}$$

$$\tilde{E} = \eta\left(\frac{m}{M}\right)^{1/2}\left(\frac{64\pi n_0 \kappa T_e}{3}\right)^{1/2}. \tag{4d}$$

Here, m, and M are the electron and ion masses, $\lambda_D = (\kappa T_e/4\pi e^2 n_0)^{1/2}$ is the Debye length, T_e the electron temperature, κ Boltzmann's constant, e the electron charge and $\eta = \gamma_e + \gamma_i T_i/T_e$, where $\gamma_{e,i}$ are the adiabatic exponents of electrons and ions.

https://doi.org/10.1017/S0022377897005886 Published online by Cambridge University Press

The parameters entering (3) are

$$\left.\begin{aligned} \boldsymbol{\Omega} &= \omega_0 - \omega_{UH}, \\ E_0 &= \mathbf{E}_0 \cdot \mathbf{e}_x, \\ \nu &= \tfrac{1}{2}\,\nu_e, \\ \boldsymbol{\Omega}_{LH} &= (\boldsymbol{\Omega}_e \boldsymbol{\Omega}_i)^{1/2} \end{aligned}\right\} \tag{5}$$

(measured in units (4)), where the upper-hybrid frequency $\omega_{UH} = (\omega_{pe}^2 + \boldsymbol{\Omega}_e^2)^{1/2}$, $\omega_{pe} = (4\pi e^2 n_0/m_e)^{1/2}$, $\boldsymbol{\Omega}_{e,i} = eB_0/m_{e,i}c$, ν_e is the electron collision frequency, $m_e = m$, $m_i = M$, B_0 is the (constant) background magnetic field and c is the velocity of light.

In Sec. 7, the set of equations (3) will be extended to the case of variations in two space dimensions perpendicular to the magnetic field. There is an important omission in the formulation (3): the upper-hybrid mode is not a purely electrostatic mode; consequently, it can leak to the Z mode in the subcritical regions outside the density depletions (Mjølhus 1983). It is a worthwhile task, not undertaken in this paper, to consider the extension of the present theory to the situation where the electromagnetic terms responsible for this leakage are retained.

3. Stationary solution

Let $\hat{E}(x)$, $\hat{n}(x)$ be a time-independent solution of (3), i.e.

$$\frac{d^2\hat{E}}{dx^2} + [\boldsymbol{\Omega} + i\nu - (\hat{n} + N)]\,\hat{E} = E_0(\hat{n} + N), \tag{6a}$$

$$\left(\frac{d^2}{dx^2} - \boldsymbol{\Omega}_{LH}^2\right)\hat{n} = -\frac{d^2}{dx^2}\,|\hat{E} + E_0|^2. \tag{6b}$$

$\hat{E}(x)$ represents the spatial structure of stationary upper-hybrid oscillations at frequency ω_0, being generated by the combined action of the pump field E_0 and the prescribed density perturbation $N(x)$. Then $\hat{n}(x)$ is the self-consistent ponderomotive modification to this situation.

We shall be particularly interested in the situation where

(i) $N(x)$ represents an isolated density depletion, $N(x) < 0$, $N(x) \to 0$ as $|x| \to \infty$;

(ii) $\boldsymbol{\Omega}$ is negative; $0 > \boldsymbol{\Omega} > \min N(x)$.

These two conditions imply that the medium is evanescent for upper-hybrid oscillations outside the striation, $N(x) - \boldsymbol{\Omega} > 0$, and allows upper-hybrid oscillations inside the region $N(x) - \boldsymbol{\Omega} < 0$ (Fig. 1*b*). Thus solutions to (6) with boundary conditions $\hat{E}(x)$, $\hat{n}(x) \to 0$ as $|x| \to \infty$ represent stationary upper-hybrid oscillations trapped by the density depletion $N + \hat{n}$. An example is shown in Fig. 1(*a*).

In order to obtain a foundation for a discussion of these stationary solutions, consider first the approximation obtained when $\hat{n}$ is neglected:

$$\frac{d^2\hat{E}}{dx^2} + [\boldsymbol{\Omega} + i\nu - N(x))]\,\hat{E} = N(x)E_0, \tag{7a}$$

$$\hat{E} \to 0 \quad \text{as} \quad |x| \to \infty. \tag{7b}$$

We shall call this the non-consistent stationary state. Since $L_N = -d^2/dx^2 + N(x)$ is

https://doi.org/10.1017/S0022377897005886 Published online by Cambridge University Press

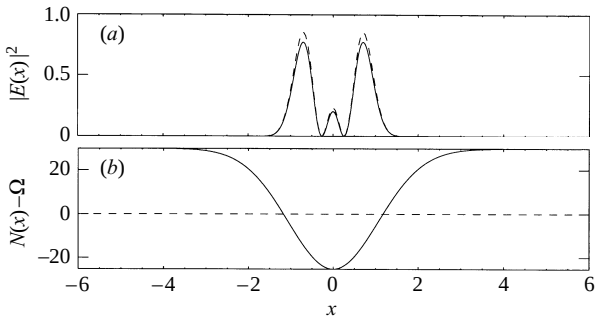


Figure 1. (*a*) Example of computed trapped upper-hybrid electric field structure $|\hat{E}(x)|^2$. (*b*) Corresponding density profile. In (*a*) the solid line is the electric field structure computed from (7) with $\Omega = -29.8$, $\nu = 0.5$, $E_0 = 0.075$, $\Omega_{LH}^2 = 375$ and $N(x)$ as described in Appendix A. The broken line was obtained by solving (A 1) for $\bar{\Omega} = -29.8$, and the remaining parameters as above, plotting $|E(x)|^2$ at $t = 40$.

a self-adjoint operator on the space of functions with boundary condition (7*b*), the eigenvalues are real. There will be at most a finite number of them, $\min N(x) < \Omega_0 < \Omega_1 < \ldots < \Omega_M < 0$. The corresponding eigenfunctions represent autonomous (e.g. undriven and undamped) standing upper-hybrid oscillations. Since the eigenvalues are real, the Fredholm-alternative theorem implies that (7) has a unique solution for $\nu \neq 0$. Using the spectral resolution of the linear operator L_N, the solution can be written as (Friedrichs 1948)

$$\hat{E}(x) = E_0 \left[\sum_{j=0}^{M} \frac{N_j}{\Omega + i\nu - \Omega_j} e_j(x) + \int_{-\infty}^{\infty} \frac{\hat{N}(k)}{\Omega + i\nu - k^2} e^+(x,k)\, dk \right]. \tag{8}$$

In the first term, deriving from the discrete spectrum of L_N, $e_j(x)$, $j = 0, ..., M$, are the normalized eigenfunctions, $\int_{-\infty}^{\infty} e_j^2(x)\, dx = 1$, and N_j are the projections of $N(x)$ onto them, $N_j = \langle N, e_j \rangle$, where we use the inner-product notation

$$\langle u, v \rangle = \int_{-\infty}^{\infty} u(x) v^*(x)\, dx.$$

The second term derives from the continuous spectrum: $e^+(x,k)$ is a solution of $L_N e = k^2 e$ satisfying the boundary condition of an outgoing wave at $+\infty$, while

$$\hat{N}(k) = \frac{1}{i\pi} \int_{-\infty}^{\infty} \frac{k e^-(x,k)}{W} N(x)\, dx,$$

where $e^-(x,k)$ satisfies the boundary condition of an outgoing wave at $-\infty$, and $W = W[e^+, e^-]$ is the Wronskian.

The solution (8) shows in particular that, for small ν, $\hat{E}(x)$ becomes particularly large when Ω is near one of the eigenvalues. We shall call these values of Ω *trapped oscillation resonances*. In Fig. 2, a graph of

$$U(\Omega) = \int |\hat{E}(x)|^2\, dx$$

(computed numerically) is shown, clearly exhibiting these resonances. Note that when $N(x)$ is an even function, the eigenfunctions $e_0, e_2, ...$ are even functions, while $e_1, e_3, ...$ are odd functions. Consequently, $N_1, N_3, \ldots$ vanish. Thus only the even

https://doi.org/10.1017/S0022377897005886 Published online by Cambridge University Press

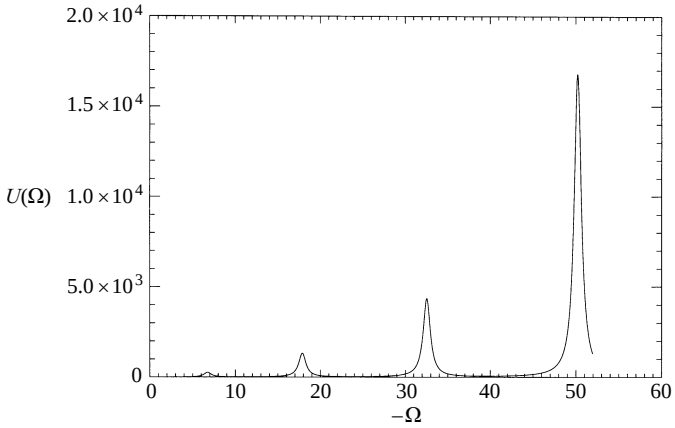


Figure 2. The trapped upper-hybrid oscillation resonances, obtained by solving (7*a*) with $\nu = 0.5$ and $E_0 = 1.0$ as described in Appendix A and computing the integral for U as a function of $\mathbf{\Omega}$. Even resonances are seen at $\mathbf{\Omega}_0 \approx -50.2$, $\mathbf{\Omega}_2 \approx -32.5$, $\mathbf{\Omega}_4 \approx -17.8$ and $\mathbf{\Omega}_6 \approx -6.8$. The odd reonances occur at $\mathbf{\Omega}_1 = -41.0$, $\mathbf{\Omega}_3 \approx -24.8$, $\mathbf{\Omega}_5 \approx -11.9$, determined numerically by replacing $N(x)$ on the right-hand side of (7*a*) by the odd function $xN(x)$.

resonances will be excited. It may also be noted that the lowest resonances are most strongly excited. The higher resonances are weaker because of the oscillations of $e_j(x)$ in the computation of N_j.

Turning now to the problem of a stationary solution (6*a*,*b*) with boundary condition $\hat{E}, \hat{n} \to 0$ as $|x| \to \infty$, it can be reformulated as a fixed-point problem

$$\hat{E}(x) = T\{\hat{E}(x)\}, \tag{9}$$

where T is the nonlinear operator

$$T\{E\} = \int_{-\infty}^{\infty} G_{\mathbf{\Omega}}(x,\xi)\,\{E_0\,[N(\xi) + \hat{n}\{E\}(\xi)] + E(\xi)\hat{n}\{E\}(\xi)\}\,d\xi,$$

where

$$\hat{n}\{E\}(x) = \tfrac{1}{2}\mathbf{\Omega}_{LH}\int_{-\infty}^{\infty} e^{-\mathbf{\Omega}_{LH}|x-x'|}[|E(x') + E_0|^2 - E_0^2]dx' - [|E(x) + E_0|^2 - |E_0|^2],$$

and $G_{\mathbf{\Omega}}(x,\xi)$ is the Green function for the operator $-L_N + \mathbf{\Omega} + i\nu$ with boundary condition (7*b*). Using standard fixed-point theorems, such as the contraction lemma, it is possible to prove that a fixed point exists for (9) for sufficiently small E_0. However, it is generally not expected that the nonlinear stationary problem has a solution for any E_0.

In order to indicate some of the richness of the nonlinear stationary problem (6), this section ends with a demonstration of the familiar hysteresis near resonances in nonlinear systems. Using perturbation method, we treat E_0 as a small parameter, and assume $\mathbf{\Omega} - \mathbf{\Omega}_j$ and ν to be of order E_0. In addition, $\mathbf{\Omega}_{LH}$ occurs as a stiffness parameter in the nonlinearity, so also $1/\mathbf{\Omega}_{LH}^2$ is assumed $O(E_0)$. We seek a solution in the form

$$\hat{E}(x) = \alpha e_j(x) + E_\perp(x),$$

where we seek the amplitude $\alpha = O(1)$, while $E_\perp$ is an $O(E_0)$ perturbation assumed

https://doi.org/10.1017/S0022377897005886 Published online by Cambridge University Press

to be in the orthogonal complement of e_j. To leading order, we have from (6*b*)

$$\hat{n}(x) = \frac{1}{2\Omega_{LH}} |\alpha|^2 \int_{-\infty}^{\infty} \hat{\chi}'(x') e^{-\Omega_{LH}|x-x'|}\, dx'$$

with $\hat{\chi}(x) = (d/dx)e_j^2(x)$. Using this in (6*a*) gives

$$(\Omega + i\nu - \Omega_j)\alpha = E_0 N_j + \chi\alpha|\alpha|^2, \tag{10}$$

where

$$\chi = \frac{1}{2\Omega_{LH}} \int_{-\infty}^{\infty}\int_{-\infty}^{\infty} \hat{\chi}(x)\hat{\chi}(x') e^{-\Omega_{LH}|x-x'|}\, dx\, dx'$$

is small of order Ω_{LH}^{-2}.

The cubic amplitude equation (10) (for α) has the usual form for nonlinear resonance (Stoker 1950). The bending of the resonance curve characteristic of hysteresis implies that the stationary response to E_0 may undergo sudden jumps as a function of the parameter Ω or E_0.

4. Linearization and approximate dispersion relation

In order to investigate the stability of the stationary solutions discussed in Sec. 3, (3) are now linearized around the stationary solution $\hat{E}(x), \hat{n}(x)$, assuming that it exists. Writing

$$E = \hat{E} + e, \qquad E^* = \hat{E}^* + e^*, \qquad n = \hat{n} + \delta, \tag{11}$$

linearizing (3) around $\hat{E}$ and $\hat{n}$, and considering a single Fourier component

$$\begin{pmatrix} e(x,t) \\ e^*(x,t) \\ \delta(x,t) \end{pmatrix} = \begin{pmatrix} e_\omega(x) \\ e^*_{-\omega}(x) \\ \delta_\omega(x) \end{pmatrix} e^{-i\omega t}, \tag{12}$$

the equations

$$(-L_{N+\hat{n}} + \Omega + \omega + i\nu)\, e_\omega = (\hat{E} + E_0)\delta_\omega, \tag{13a}$$

$$(-L_{N+\hat{n}} + \Omega - \omega - i\nu)\, e^*_{-\omega} = (\hat{E}^* + E_0^*)\delta_\omega, \tag{13b}$$

$$D_\lambda \delta_\omega = \frac{d^2}{dx^2}[(\hat{E}^* + E_0^*)e_\omega + (\hat{E} + E_0)e^*_{-\omega}] \tag{13c}$$

are obtained, where the operators L_n and D_λ are defined as

$$L_n = -\frac{d^2}{dx^2} + n(x), \tag{14a}$$

$$D_\lambda = -\frac{d^2}{dx^2} + \lambda^2, \tag{14b}$$

where in (13*c*) $\lambda^2 = \Omega_{LH}^2 - \omega^2$. Note that, since $E(x,t)$ in (3) is already complex by virtue of (2), we have to treat $e_\omega(x)$ and the antiStokes component $e^*_{-\omega}(x)$ as independent.

The ultimate goal is to determine the values of ω that, for given values of Ω, ν and E_0, permit (13) to have a solution bounded as $|x| \to \infty$. This will be called a 'dispersion relation', although this may not be fully appropriate, since no wavenumber appears. In order to obtain an approximate dispersion relation, we approximate

https://doi.org/10.1017/S0022377897005886 Published online by Cambridge University Press

the exact solution with one in the space spanned by the (normalized) eigenvectors $\hat{e}_1(x), \ldots, \hat{e}_M(x)$ of the operator $L_{N+\hat{n}}$:

$$L_{N+\hat{n}}\hat{e}_j = \hat{\Omega}_j \hat{e}_j, \qquad j = 0, \ldots, M. \tag{15}$$

Again, the $\hat{\Omega}_j$ are negative, $\min(N+\hat{n}) < \hat{\Omega}_j < 0$, and $\hat{\Omega}_j \to \Omega_j$, $\hat{e}_j \to e_j$ as $E_0 \to 0$. We now approximate the solution of (13) with a projection onto the space spanned by $\hat{e}_1, \ldots, \hat{e}_M$:

$$e_\omega \approx \sum_{j=0}^{M} \alpha_{\omega,j}\hat{e}_j, \qquad e^*_{-\omega} \approx \sum_{j=0}^{M} \alpha^*_{-\omega,j}\hat{e}_j, \tag{16}$$

where $\alpha_{\omega,j}$ and $\alpha^*_{-\omega,j}$ are unknown complex numbers (i.e. we apply a Galerkin-type method). Inserting this into (13*a*,*b*) gives

$$\alpha_{\omega,j} = \frac{X_j}{\omega + i\nu + \Omega - \hat{\Omega}_j}, \tag{17a}$$

$$\alpha^*_{-\omega,j} = \frac{Y_j}{-\omega - i\nu + \Omega - \hat{\Omega}_j}, \tag{17b}$$

$$X_j = \int_{-\infty}^{\infty} (\hat{E} + E_0)\delta_\omega \hat{e}_j \, dx, \tag{17c}$$

$$Y_j = \int_{-\infty}^{\infty} (\hat{E}^* + E_0^*)\delta_\omega \hat{e}_j \, dx. \tag{17d}$$

The solution to (13*c*) for $|\omega| < \Omega_{LH}$ can be written as

$$\delta_\omega(x) = \frac{\lambda}{2}\int_{-\infty}^{\infty} e^{-\lambda|x-x'|}F(x')dx' - F(x), \tag{18}$$

with

$$F(x) = [\hat{E}(x) + E_0]e^*_{-\omega}(x) + [\hat{E}^*(x) + E_0^*]e_\omega(x).$$

We now (i) insert (16) and (17) into (18), and (ii) multiply (18) by $[\hat{E}(x) + E_0]\hat{e}_j(x)$ and integrate from $-\infty$ to ∞, and similarly with $[\hat{E}^*(x) + E_0^*]\hat{e}_j(x)$; then a linear algebraic system of equations for X_j and Y_j, valid for $|\omega| < \Omega_{LH}$, is obtained:

$$X_i = \sum_{j=0}^{M} \frac{|E_0|^2 W_{ij}}{D_{\omega,j}} X_j + \sum_{j=0}^{M} \frac{|E_0|^2 \tilde{W}_{ij}}{D^*_{-\omega,j}} Y_j, \tag{19a}$$

$$Y_i = \sum_{j=0}^{M} \frac{|E_0|^2 \tilde{W}^*_{ij}}{D_{\omega,j}} X_j + \sum_{j=0}^{M} \frac{|E_0|^2 W^*_{ij}}{D^*_{-\omega,j}} Y_j, \tag{19b}$$

$i = 1, \ldots, M$, where (for $|\omega| < \Omega_{LH}$)

$$|E_0|^2 W_{ij} = \frac{\lambda}{2}\int_{-\infty}^{\infty}\int_{-\infty}^{\infty} V_i(x)V_j^*(x')e^{-\lambda|x-x'|}\,dx\,dx' - \int_{-\infty}^{\infty} V_i(x)V_j^*(x)\,dx, \tag{20a}$$

$$|E_0|^2 \tilde{W}_{ij} = \frac{\lambda}{2}\int_{-\infty}^{\infty}\int_{-\infty}^{\infty} V_i(x)V_j(x')e^{-\lambda|x-x'|}\,dx\,dx' - \int_{-\infty}^{\infty} V_i(x)V_j(x)\,dx, \tag{20b}$$

$$V_j(x) = [\hat{E}(x) + E_0]\hat{e}_j(x), \tag{20c}$$

$$\left.\begin{aligned} D_{\omega,j} &= \omega + i\nu + \Omega - \hat{\Omega}_j, \\ D^*_{-\omega,j} &= -\omega - i\nu + \Omega - \hat{\Omega}_j\,. \end{aligned}\right\} \tag{20d}$$

https://doi.org/10.1017/S0022377897005886 Published online by Cambridge University Press

The scaling with $|E_0|^2$ in the definitions of W_{ij} and $\tilde{W}_{ij}$ has been chosen so that they become independent of E_0 in the small-E_0 limit where the non-consistent equilibrium (7) can be used. In the one-dimensional case, one can, with no loss of generality, assume E_0 to be real and positive, which will be done henceforth.

When $\nu = 0$, $\hat{E}$ is real-valued. Then $W_{ij} = \tilde{W}_{ij}$, they are real-valued for $|\omega| < \Omega_{LH}$, and $X_i = Y_i$. Then (19) reduces to

$$X_i = E_0^2 \sum_{j=1}^{n} W_{ij} \left(\frac{1}{D_{\omega,j}} + \frac{1}{D_{-\omega,j}} \right) X_j.$$

For $|\omega| > \Omega_{LH}$, the appropriate matrices W_{ij} and $\tilde{W}_{ij}$ are obtained by continuing λ via the upper complex ω half-plane, which is the appropriate choice to preserve causality. Note that then the matrices W_{ij}^* and $\tilde{W}_{ij}^*$ of (19*b*) are no longer the complex conjugates of W_{ij} and $\tilde{W}_{ij}$.

The sought 'dispersion relation' is now the determinant of the system (19). One could, in principle, extend it to an exact representation of the linearized problem (13), by also including contributions from the continuous spectrum, as in (8). This would turn (19) into a set of integral equations. However, this is not found worthwhile, because what are needed in the two next sections are rather crude approximations to (19).

5. The trapped oscillations decay instability

Consider the case when E_0 is small. To leading order, one has the 'dispersion relations' $\omega = -i\nu + \hat{\Omega}_l - \Omega$. For each l, this gives the frequency of a weakly damped trapped mode l. If one wishes to extend one of these up to order E_0^2, one gets from (19)

$$\omega = -i\nu + \hat{\Omega}_l - \Omega + E_0^2 W_{ll}(\omega), \tag{21}$$

where $W_{ll}(\omega)$ is defined in (20). It is readily seen that involving off-diagonal terms in (19) will imply terms of order E_0^4, so (21) is the only alternative including terms up to this order.

For ω real and $|\omega| < \Omega_{LH}$, W_{ll} is real-valued. Continuing W_{ll} to $\omega < -\Omega_{LH}$ via the upper complex ω half-plane, one has for $\omega < -\Omega_{LH}$ that $\lambda = i\chi$, $\chi = (\omega^2 - \Omega_{LH}^2)^{1/2}$, so that, for real ω, $\omega < -\Omega_{LH}$,

$$E_0^2 W_{ll} = E_0^2 \big(W_{ll}^{(r)} + i W_{ll}^{(i)} \big),$$

where the real part is

$$E_0^2 W_{ll}^{(r)} = \frac{\chi}{2} \int_{-\infty}^{\infty} \int_{-\infty}^{\infty} V(x) V^*(x') \sin \chi |x - x'| \, dx \, dx' - \int_{-\infty}^{\infty} |V(x)|^2, \tag{22}$$

and the imaginary part is

$$\begin{aligned} E_0^2 W_{ll}^{(i)} &= \frac{\chi}{2} \int_{-\infty}^{\infty} \int_{-\infty}^{\infty} V(x) V^*(x') \cos \chi (x - x') \, dx \, dx' \\ &= \tfrac{1}{4} \chi [|\hat{V}(\chi)|^2 + |\hat{V}(-\chi)|^2], \end{aligned} \tag{23}$$

where $\hat{V}(\chi) = \int_{-\infty}^{\infty} V(x) e^{i\chi x} \, dx$. Equation (23) shows that W_{ll} has positive imaginary part for $\omega < -\Omega_{LH}$. (For $\omega > \Omega_{LH}$, it will be negative.) On the other hand,

https://doi.org/10.1017/S0022377897005886 Published online by Cambridge University Press

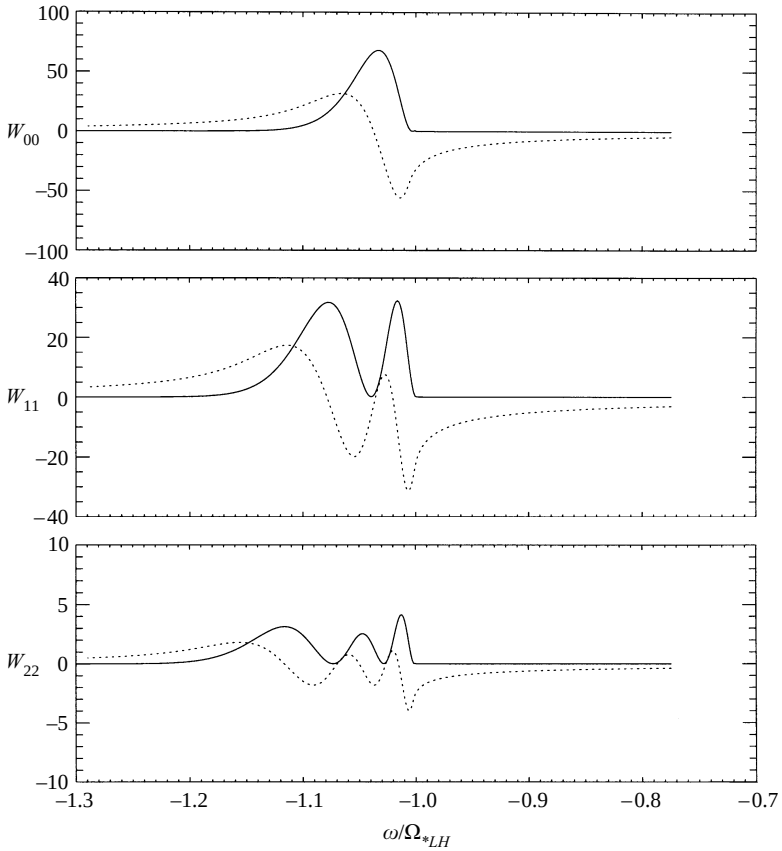


Figure 3. Three examples of $W_{ll}(\omega)$ as defined by (22) and (23). (*a*) W_{00} ($\mathbf{\Omega} = -29.8$); (*b*) W_{11} ($\mathbf{\Omega} = -20.0$); (*c*) W_{22} ($\mathbf{\Omega} = -10.8$); ——, $W_{ll}^{(i)}$; · · · · · ·, $W_{ll}^{(r)}$. In all cases, $\nu = 0.5$, and $N(x)$ and the method of computation are as described in Appendix A.

by the Riemann–Lebesgue lemma, $W_{ll}^{(i)} \to 0$ as $\omega \to -\infty$ (i.e. $\chi \to \infty$). For example, when $N + \hat{n}$ is smooth (infinitely differentiable), $\hat{V}(\chi) \to 0$ as $\chi \to \infty$ more rapidly than χ^{-p} for any positive p. In Fig. 3, some examples of $W_{ll}(\omega)$ are shown, computed for the non-consistent stationary solution and eigenfunctions.

These properties show that, for small ν, (21) predicts an instability, i.e. solutions ω may possess a positive imaginary part

$$\omega_i \approx E_0^2 W_{ll}^{(i)}(\omega_r) - \nu, \tag{24}$$

where ω_r is given implicitly by

$$\omega_r = \hat{\mathbf{\Omega}}_l - \mathbf{\Omega} + E_0^2 W_{ll}^{(r)}(\omega_r) \approx \hat{\mathbf{\Omega}}_l - \mathbf{\Omega} \tag{25}$$

((24) and (25) are valid for small ω_i). Equation (25), together with the properties of W_{ll}, shows that, for small ν and E_0, this instability can be excited when $\hat{\mathbf{\Omega}}_l - \mathbf{\Omega} \lesssim -\mathbf{\Omega}_{LH}$, and that $\omega_r \lesssim -\mathbf{\Omega}_{LH}$.

No 'wavenumber' matching condition has been inherent in the description so far. Using WKB formulae for $\hat{E}(x)$ and $e_l(x)$, wavenumber matching conditions would occur as stationary-phase conditions for the computation of the integral for

https://doi.org/10.1017/S0022377897005886 Published online by Cambridge University Press

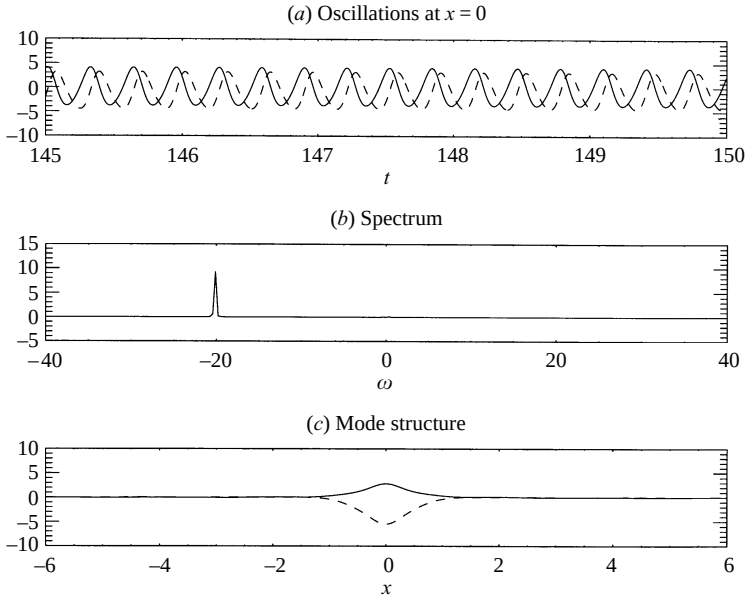


Figure 4. Example of TOD instability. All parameters are as in Fig. 1, except that $E_0 = 0.15$. (*a*) Oscillations of $E(0)$: ——, $\mathrm{Re}(E)$; ·····, $\mathrm{Im}(E)$; (*b*) Spectrum $|E(0,\omega)|^2$, where $E(0,\omega)$ is the discrete Fourier transform of $E(0,t)$ for $130 \leqslant t \leqslant 150$. (*c*) Mode structure $E(x,t+\Delta t) - E(x,t)$ for $t = 150.075$, $\Delta t = 0.075$. The data were obtained by solving (A 1) as described in Appendix A. For $0 \leqslant t \leqslant 40$, $E_0 = 0.075$; for $40 \leqslant t \leqslant 120$, $E_0 = 0.1$; for $120 \leqslant t \leqslant 150.15$, $E_0 = 0.15$.

$E_0^2 W_{ll}^{(i)}(\omega)$. For χ in a certain interval, two points of stationary phase will occur when $N(x)$ is localized and monotone on each side of its minimum: one on each side. The oscillations in $W_{ll}^{(i)}$, as seen in Fig. 3, can be explained as constructive versus destructive phase differences between these two contributions. When χ is outside the interval where stationary-phase points occur, $E_0^2 W_{ll}^{(i)}$ decays rapidly, as seen in Fig. 3.

In Fig. 4, an example is shown of the excitation of the TOD instability. For the first 40 time units, the parameters were as in Fig. 1, and the stationary state was approached. For $40 < t \leqslant 120$, $E_0 = 0.1$, for which small sustained oscillations persisted. For $120 < t < 150$, $E_0 = 0.15$. The data in Fig. 4 are from this t interval, where significant though very regular oscillations persisted. In Fig. 4(*a*), the very regular character of the oscillations is apparent, while the spectrum $|E(0,\omega)|^2$ in Fig. 4(*b*) shows that the downshift is $\omega \approx -20.2$, which is slightly below $-\boldsymbol{\Omega}_{LH} = -19.36$. The mode is a decay to the lowest trapped oscillation resonance at $\omega \approx \boldsymbol{\Omega}_0 - \boldsymbol{\Omega}$, where $\boldsymbol{\Omega}_0 \approx -50.2$ (Fig. 2) and $\bar{\boldsymbol{\Omega}} = -29.8$ in the computation (see Appendix A for the definition of $\bar{\boldsymbol{\Omega}}$). This interpretation is supported by Fig. 4(*c*), which shows $E(x,t_0+\Delta t) - E(x,t_0)$, where Δt was chosen as about a quarter of an oscillation period. The mode structure is conveniently exhibited this way; $E(x,t)$ also contains the (unstable) stationary structure $\hat{E}(x)$, which is filtered out by taking this difference.

Figure 5 shows an example of a decay to an odd resonance; even if the odd resonances do not show up in the stationary states, they can be the products of a decay instability. Also in this case, the frequency is downshifted ($\omega \approx -21$, Fig. 5(*b*),

https://doi.org/10.1017/S0022377897005886 Published online by Cambridge University Press

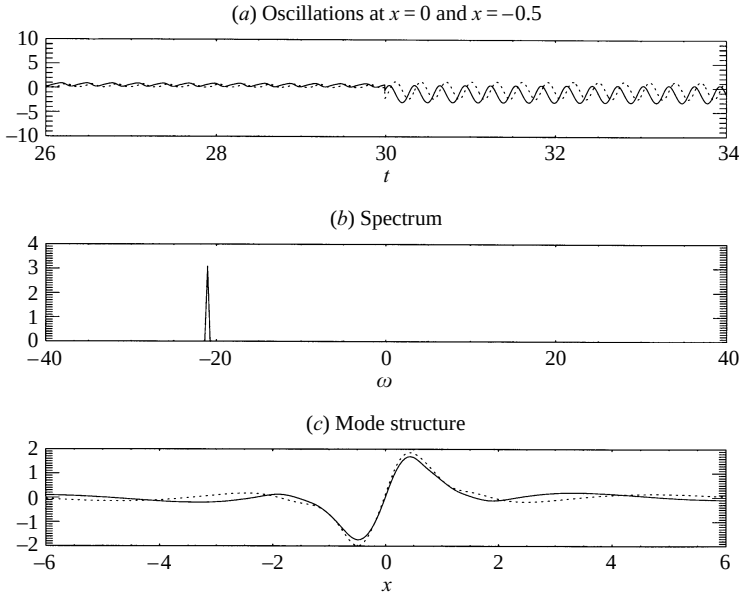


Figure 5. TOD instability to odd mode. The parameters $\Omega = -20$, $\nu_e = 0.5$ and $E_0 = 0.2$. For $0 \leqslant t \leqslant 30$, E was sampled in $x = 0$, while for $30 < t \leqslant 50$, E was sampled in $x = -0.5$. (*a*) Real (——) and imaginary ($\cdots\cdots$) parts of $E(\xi_0, t)$ for $\xi_0 = 0$ ($t < 30$) and $\xi_0 = -0.5$ ($t > 30$). (*b*) Spectrum $|\hat{E}(\xi_0, \omega)|^2$, $30 \leqslant t \leqslant 50$. (*c*) Mode structure $E(x, t_0 + \Delta t) - E(x, t_0)$ for $t_0 = 50$, $\Delta t = 0.075$.

$\bar{\Omega} = -20$, $\Omega_1 \approx -41$), and $\omega \approx \Omega - \Omega_1$ at the same time as $\omega \lesssim -\Omega_{LH}$. Figure 5(*c*) again identifies the mode structure as the lowest odd (antisymmetric) mode.

6. The Stokes–antiStokes instability

It is readily seen that when one denominator $D_{\omega,l}$ in (19) is small, i.e. $\omega \approx -(\Omega - \hat{\Omega}_l)$, then the other $D_{\omega,j}$, $j \neq l$, are not simultaneously small. However, it is possible to have $D^*_{-\omega,m}$ small when $\omega \approx \Omega - \hat{\Omega}_m$; this may occur when $\Omega \approx \frac{1}{2}(\hat{\Omega}_l + \hat{\Omega}_m)$ and $\omega \approx \frac{1}{2}(\hat{\Omega}_l - \hat{\Omega}_m)$. Assuming E_0^2 to be small, it is reasonable to retain exactly the terms with resonant denominators on the right-hand sides of (19). From this, the 'dispersion relation'

$$\left(1 - \frac{E_0^2 W_{ll}}{D_{\omega,l}}\right)\left(1 - \frac{E_0^2 W_{mm}}{D^*_{-\omega,m}}\right) - \frac{E_0^4 |\tilde{W}_{lm}|^2}{D_{\omega,l} D^*_{-\omega,m}} = 0 \tag{26}$$

is obtained. Introducing

$$\tilde{\omega}_j = \hat{\Omega}_j - \Omega + E_0^2 W_{jj}(\omega)\,, \qquad j = l, m, \tag{27}$$

this can be written as

$$(\omega - \tilde{\omega}_l + i\nu)(\omega + \tilde{\omega}_m + i\nu) = -E_0^4 |\tilde{W}_{lm}|^2\,. \tag{28}$$

It can readily be demonstrated that (28) predicts an instability when Ω is properly adjusted. We shall restrict ourselves to the range $|\omega| < \Omega_{LH}$, so that λ is real.

https://doi.org/10.1017/S0022377897005886 Published online by Cambridge University Press

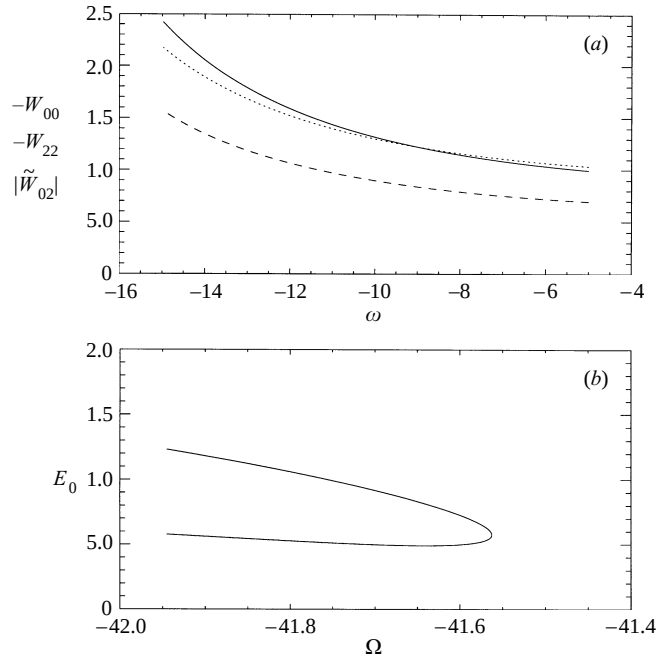


Figure 6. (*a*) The functions $-W_{00}(\omega)$ (——), $-W_{22}(\omega)$ (· · · · · ·) and $|\tilde{W}_{02}(\omega)|$ (- - - - - -), computed for $\Omega = -41.35$ and $\nu_e = 0.2$ (non-consistent model (7)). (*b*) The threshold curve for the S–aS instability between the 0th and the 2nd resonance, $\nu_e = 0.2$. The method is described in Appendix A.

Adjusting Ω such that $\tilde{\omega}_l = -\tilde{\omega}_m$, implying

$$\Omega = \hat{\Omega}_0 - cE_0^2, \tag{29}$$

with $\hat{\Omega}_0 = \frac{1}{2}(\hat{\Omega}_l + \hat{\Omega}_m)$ and $c = -\frac{1}{2}(W_{ll} + W_{mm})$, the left-hand side of (28) with $\nu = 0$ has a double root

$$\omega = \omega_0 + \tfrac{1}{2}E_0^2(W_{ll} - W_{mm}), \tag{30}$$

with $\omega_0 = \frac{1}{2}(\hat{\Omega}_l - \hat{\Omega}_m)$. Then, retaining the right-hand side of (28), this double root splits into two complex-conjugate roots with imaginary parts $\pm iE_0^2|\tilde{W}_{lm}|$; thus an instability is predicted. Retaining the damping ν, the threshold condition

$$\nu = E_{0,t}^2|\tilde{W}_{lm}|$$

is obtained.

It turns out that this is the smallest threshold obtainable, valid when (29) is satisfied. More generally, a threshold relation between Ω and E_0 can be obtained by requiring that (28) have real ω. Then again, (30) is obtained, while

$$(\Omega - \hat{\Omega}_0 + cE_0^2)^2 = E_0^4a^2 - \nu^2, \qquad a = |\tilde{W}_{lm}| \tag{31}$$

gives the relation between E_0 and Ω. From the results of Appendix B, $c \geqslant 0$ and $c^2 \geqslant a^2$. It follows from these two conditions that the threshold curve will generally

https://doi.org/10.1017/S0022377897005886 Published online by Cambridge University Press

look like Fig. 6(*b*):

(i) there is a largest value of Ω, $\Omega = \hat{\Omega}_0 - (\nu/a)(c^2 - a^2)^{1/2}$, at which the threshold curve has a vertical tangent;

(ii) to the left of this point, (31) gives two positive values of E_0 for each value of Ω, and thus, the instability only exists between these two values.

In Fig. 6(*a*), examples of the functions $W_{00}(\omega)$, $W_{22}(\omega)$ and $|\tilde{W}_{02}(\omega)|$ are shown for a range of values of ω for which λ is real. In Fig. 6(*b*), the threshold curve has been computed for the corresponding case. These results have been computed using the non-consistent stationary solution and eigenfunctions.

In Fig. 7, a numerical example of the S–aS instability is shown for the same situation as in Fig. 6. Equation (A 1) from Appendix A were solved numerically, and the numerical calculations were continued at increasing values of E_0. In Fig. 7(*a*), the time variation of $W = \sum_k |E(k,t)|^2$ is shown for increasing values of E_0. At $E_0 = 0.4$ ($0 < t \leqslant 50$), slowly damped oscillations occur, while at $E_0 = 0.55$ ($50 \leqslant t \leqslant 80.18$), there are sustained oscillations. At $E_0 = 0.7$, the oscillations are again damped. Thus, in this case, the qualitative picture seen in Fig. 6(*b*) is verified: the instability exists only between a lower and an upper value of E_0. In Fig. 7(*b*), the oscillations at $x = 0$ are exhibited. In Fig. 7(*c*), $|E(0,\omega)|^2$ is shown, where $E(0,\omega)$ is the (discrete) Fourier transform of $E(x = 0, t)$ for $60 \leqslant t \leqslant 80$. The spectral peaks are situated at $\omega \approx \pm 8.85$, which is the value predicted by (30). Unlike the cases of Figs 4 and 5, the upshifted (antiStokes) line is also significant in this instability. In Fig. 7(*c*), the difference $E(x,t_2) - E(x,t_1)$ is shown, where $t_2 - t_1 = 0.18$ is about a quarter of an oscillation period. There are slight deviations between the threshold curve of Fig. 6(*b*) and the numerical results obtained. The lowest threshold is slightly lower, and the instability exists at higher values of $\bar{\Omega}$. The example of Fig. 7 was computed for $\bar{\Omega} = -41.55$, which is the highest value (vertical tangent) in Fig. 6(*b*). Similar behaviour resulted at $\bar{\Omega} = -41.45$, while no instability occurred at $\bar{\Omega} = -41.35$. The occurrence of an upper limit for E_0 as well as a lower threshold, as predicted by Fig. 6(*b*), could only be numerically demonstrated sufficiently near the tip of the threshold curve of Fig. 6(*b*). In Mjølhus and Helmersen (1997), a numerical example was shown in which very violent aperiodic broad-spectrum oscillations developed at $E_0 = 0.8$.

For the case where the striation profile $N(x)$ is an even function, the two resonances participating in the S–aS instability must either both be even or both odd: for the case of a mixture of an odd and an even resonance, $\tilde{W}_{lm}$ is readily proved to vanish.

7. Two-dimensional geometry

The theory has so far been described for the case of slab geometry, because this is the easiest to handle mathematically; also, it is for this case that the instabilities have been demonstrated numerically. However, in ionospheric experiments, one rather expects the striations to be two-dimensional: $N = N(\mathbf{x})$ where $\mathbf{x} = (x, y)$ are coordinates in the plane perpendicular to ambient magnetic field, and $N \to 0$ as $|\mathbf{x}| \to \infty$. In this section, it will be demonstrated that the structure of the theory is very much the same as for the one-dimensional case.

https://doi.org/10.1017/S0022377897005886 Published online by Cambridge University Press

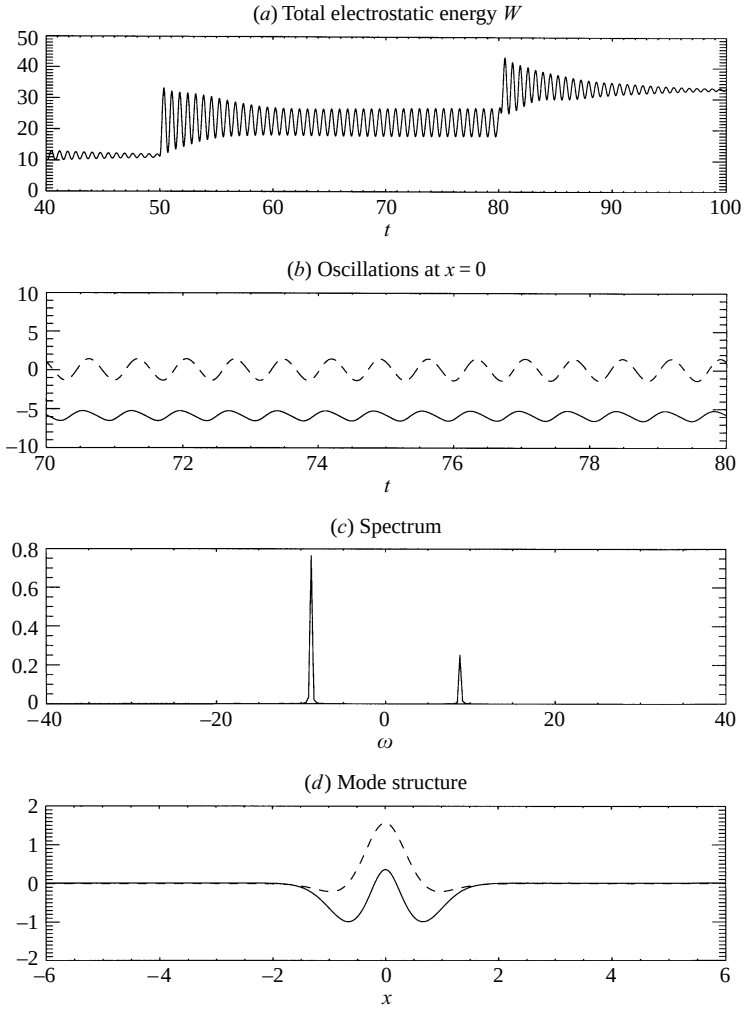


Figure 7. Example of Stokes–antiStokes instability. Equations (A 1) were solved with parameters $\bar{\Omega} = -41.55$ and $\nu_e = 0.2$, and numerical parameters as described in Appendix A. For $0 < t \leqslant 50$, $E_0 = 0.4$; for $50 < t \leqslant 80.18$, $E_0 = 0.55$; for $80.18 < t \leqslant 110$, $E_0 = 0.7$. (*a*) The total electrostatic energy $W = \sum |E(k)|^2$ as a function of t, for $40 \leqslant t \leqslant 100$. (*b*) Oscillations of $E(x = 0, t)$ for $70 < t < 80$: ——, $\mathrm{Re}\,(E)$; - - - - - -, $\mathrm{Im}\,(E)$. (*c*) $|E(0, \omega)|^2$, where $E(0, \omega)$ is the discrete Fourier transform of $E(0, t)$ for $60 \leqslant t \leqslant 80$. (*d*) Mode structure $E(x, t_2) - E(x, t_1)$, where $t_2 = 80.18$ and $t_1 = 80$: ——, $\mathrm{Re}(E)$; - - - - - -, $\mathrm{Im}(E)$.

The governing equations in this case are

$$\boldsymbol{\nabla} \cdot \{i(\partial_t + \nu)\boldsymbol{\nabla}\phi + \nabla^2\boldsymbol{\nabla}\phi + [\boldsymbol{\Omega} - (n + N)]\boldsymbol{\nabla}\phi\} = \boldsymbol{\nabla} \cdot [(n + N)\mathbf{E}_0], \tag{32a}$$

$$\frac{\partial^2 n}{\partial t^2} - \nabla^2 n + \boldsymbol{\Omega}_{LH}^2 n = \nabla^2 |\mathbf{E}_0 + \boldsymbol{\nabla}\phi|^2, \tag{32b}$$

where $\boldsymbol{\nabla} = \mathbf{e}_x(\partial/\partial x) + \mathbf{e}_y(\partial/\partial y)$ is the gradient operator in the plane perpendicular to the ambient magnetic field, and the electrostatic field complex amplitude is $\mathbf{E} = \boldsymbol{\nabla}\phi$. The driving electric field complex amplitude vector $\mathbf{E}_0$ is assumed spatially constant. The units are defined in (4).

https://doi.org/10.1017/S0022377897005886 Published online by Cambridge University Press

We first take a look at the stationary state. For each $n(\mathbf{x})$, we can define the differential operator L_n by

$$L_n = -\nabla^2 + n, \tag{33}$$

and, for each positive λ, we can define

$$D_\lambda = -\nabla^2 + \lambda^2 . \tag{34}$$

The stationary state $\boldsymbol{\nabla}\hat{\phi}(\mathbf{x})$, $\hat{n}(\mathbf{x})$ is then the solution to

$$\boldsymbol{\nabla} \cdot \{[L_{N+\hat{n}} - (\boldsymbol{\Omega} + i\nu)]\, \boldsymbol{\nabla}\hat{\phi}\} = -\boldsymbol{\nabla} \cdot [(\hat{n} + N)\mathbf{E}_0]\,, \tag{35a}$$

$$D_{\Omega_{LH}}\hat{n} = \nabla^2 |\mathbf{E}_0 + \boldsymbol{\nabla}\hat{\phi}|^2, \tag{35b}$$

subject to the boundary conditions $\hat{n}$, $\boldsymbol{\nabla}\hat{\phi} \to 0$ as $|\mathbf{x}| \to \infty$. We have no proof that such a solution exists, but we shall assume that it does and is unique for $\nu \neq 0$ and $|\mathbf{E}_0|$ sufficiently small. Again, we shall use the non-self-consistent approximation

$$\boldsymbol{\nabla} \cdot \{[L_N - (\boldsymbol{\Omega} + i\nu)]\, \boldsymbol{\nabla}\hat{\phi}\} = -\boldsymbol{\nabla} \cdot (N\mathbf{E}_0) \tag{36}$$

as a reference case, but, unlike the one-dimensional case, we do not have a proof of even the existence of a solution in this case.

For both the issue of a stationary solution, and our later treatment of the stability issue, it is necessary to characterize the somewhat non-standard Hermitian structure associated with the operator L_n. We use an inner product of vector fields $\mathbf{F}(\mathbf{x})$ and $\mathbf{G}(\mathbf{x})$,

$$\langle \mathbf{F}, \mathbf{G} \rangle = \iint_{\mathbb{R}^2} \mathbf{F}(x) \cdot \mathbf{G}(\mathbf{x})\, d^2\mathbf{x}.$$

In our application, the vector fields will usually be gradients of scalar fields:

$$\begin{aligned} \langle \boldsymbol{\nabla}\phi, \boldsymbol{\nabla}\psi \rangle &= \iint_{\mathbb{R}^2} \boldsymbol{\nabla}\phi \cdot \boldsymbol{\nabla}\psi\, d^2\mathbf{x} \\ &= -\iint_{\mathbb{R}^2} \phi\nabla^2\psi\, d^2\mathbf{x} = -\int_{\mathbb{R}^2} \psi\nabla^2\phi\, d^2\mathbf{x}. \end{aligned} \tag{37}$$

We shall assume that trapped modes in a density depletion $N(\mathbf{x})$ exist; they satisfy

$$\boldsymbol{\nabla} \cdot \left(L_N \boldsymbol{\nabla}\varphi_j - \boldsymbol{\Omega}_j \boldsymbol{\nabla}\varphi_j\right) = 0,$$

with boundary condition $\boldsymbol{\nabla}\varphi_j \to 0$ as $|\mathbf{x}| \to \infty$. We call $\boldsymbol{\nabla}\varphi_j(\mathbf{x})$ an eigenmode of the density depletion $N(\mathbf{x})$ and $\boldsymbol{\Omega}_j$ the corresponding eigenvalue. Using the above inner product, it is readily proved in the usual way that

(i) the eigenvalues $\boldsymbol{\Omega}_j$ are real;

(ii) the eigenmodes belonging to different eigenvalues are mutually orthogonal.

Using this inner-product structure, one can straightforwardly demonstrate the trapped mode resonances in the stationary solutions, which can occur when $\boldsymbol{\Omega}$ is near an eigenvalue and ν is small, using (36).

In the one-dimensional case, a symmetric case distinguished by even N, $N(-x) = N(x)$, showed some specific properties. In the two-dimensional case, the analogous role is played by rotational symmetry: $N = N(r)$, $r = (x^2 + y^2)^{1/2}$. The eigenmodes may break this symmetry; this symmetry breaking is characterized by the

https://doi.org/10.1017/S0022377897005886 Published online by Cambridge University Press

azimuthal mode number m. The mode number $j \mapsto (k, m)$, with k the radial mode number, and

$$\varphi_j(\mathbf{x}) = \varphi_{k,m}(r)(c_1 \cos m\theta + c_2 \sin m\theta).$$

Thus the eigenspace is two-dimensional (spanned by $\cos m\theta$ and $\sin m\theta$). For the one-dimensional case, the symmetric (even) $N(x)$ implied that the non-consistent equilibrium $\hat{E}(x)$ was also even. Connected with this, only even trapped mode resonances occurred in the stationary solutions. The corresponding structure for the non-consistent equilibrium (36) is as follows.

(i) The right-hand side of (36) has an $m = 1$ structure. Consequently, the stationary response $\hat{\phi}$ also has $m = 1$.

(ii) Consequently, only $m = 1$ resonances are excited in the stationary response.

For the consistent stationary state determined by (35), it should be noted that, given that N is rotationally symmetric, $\hat{n}$ will break this symmetry, though, for sufficiently small E_0, this symmetry-breaking perturbation can be neglected.

After these remarks on the stationary solutions and the eigenmode structure, we turn to the issue of stability of the stationary response $\boldsymbol{\nabla}\hat{\phi}, \hat{n}$. To this end, we linearize around the stationary response and Fourier-analyse:

$$\boldsymbol{\nabla}\phi = \boldsymbol{\nabla}\hat{\phi} + \boldsymbol{\nabla}\varphi_\omega \exp(-i\omega t) + \boldsymbol{\nabla}\varphi_{-\omega} \exp(i\omega t), \tag{38a}$$

$$n = \hat{n} + \delta_\omega \exp(-i\omega t) + \text{c.c.} \tag{38b}$$

The linearized equations can be written as

$$\boldsymbol{\nabla} \cdot \{[-L_{N+\hat{n}} + (\boldsymbol{\Omega} + \omega + i\nu)]\, \boldsymbol{\nabla}\varphi_\omega\} = \boldsymbol{\nabla} \cdot [(\mathbf{E}_0 + \boldsymbol{\nabla}\hat{\phi})\delta_\omega], \tag{39a}$$

$$\boldsymbol{\nabla} \cdot \{[-L_{N+\hat{n}} + (\boldsymbol{\Omega} - \omega - i\nu)]\boldsymbol{\nabla}\varphi^*_{-\omega}\} = \boldsymbol{\nabla} \cdot [(\mathbf{E}_0^* + \boldsymbol{\nabla}\phi^*)\delta_\omega], \tag{39b}$$

$$D_\lambda \delta_\omega = \nabla^2 F, \tag{39c}$$

$$F = (\mathbf{E}_0 + \boldsymbol{\nabla}\hat{\phi}) \cdot \boldsymbol{\nabla}\varphi^*_{-\omega} + (\mathbf{E}_0^* + \boldsymbol{\nabla}\hat{\phi}^*) \cdot \boldsymbol{\nabla}\varphi_\omega, \tag{39d}$$

$$\lambda^2 = \boldsymbol{\Omega}^2_{LH} - \omega^2. \tag{39e}$$

Proceeding similarly to Sec. 4, the solution of (39*a*,*b*) is approximated by a projection onto the space spanned by the eigenmodes φ_j, treating δ_ω as known; the result of this is expressed as

$$\boldsymbol{\nabla}\varphi_\omega = \sum_j \frac{X_j}{D_{j,\omega}} \boldsymbol{\nabla}\varphi_j, \tag{40a}$$

$$\boldsymbol{\nabla}\varphi^*_{-\omega} = \sum_j \frac{Y_j}{D^*_{j,-\omega}} \boldsymbol{\nabla}\varphi_j, \tag{40b}$$

where $D_{j,\omega}$ and $D^*_{j,-\omega}$ are the same as in (20*d*), while the expressions for X_j and Y_j are

$$X_j = \iint_{\mathbb{R}^2} \delta_\omega(\mathbf{x}) V_j(\mathbf{x})\, d^2\mathbf{x}, \tag{41a}$$

$$Y_j = \iint_{\mathbb{R}^2} \delta_\omega(\mathbf{x}) V^*_j(\mathbf{x})\, d^2\mathbf{x}, \tag{41b}$$

https://doi.org/10.1017/S0022377897005886 Published online by Cambridge University Press

with

$$V_j(\mathbf{x}) = (\mathbf{E}_0 + \boldsymbol{\nabla}\hat{\phi}) \cdot \boldsymbol{\nabla}\varphi_j. \tag{42}$$

The solution of (39c) is

$$\delta_\omega(\mathbf{x}) = \frac{\lambda^2}{2\pi} \iint\limits_{\mathbb{R}^2} K_0(\lambda|\mathbf{x}-\mathbf{x}'|)F(\mathbf{x}')\, d^2\mathbf{x}' - F(\mathbf{x}), \tag{43}$$

where K_0 is a standard modified Bessel function defined in Abramowitz and Stegun (1965).

Multiplying (43) by $V_j(\mathbf{x})$ and integrating over $\mathbf{x}$, and then multiplying by $V_j^*(\mathbf{x})$ and integrating over $\mathbf{x}$, one arrives at a set of homogeneous linear equations for X_j and Y_j that are formally the same as (19), but with W_{ij} and $\tilde{W}_{ij}$ now defined as

$$E_0^2 W_{ij} = \frac{\lambda^2}{2\pi} \iiiint\limits_{\mathbb{R}^2\times\mathbb{R}^2} V_i(\mathbf{x})V_j^*(\mathbf{x}')K_0(\lambda|\mathbf{x}-\mathbf{x}'|)\, d^2\mathbf{x}\, d^2\mathbf{x}' - \iint\limits_{\mathbb{R}^2} V_i(\mathbf{x})V_j^*(\mathbf{x})\, d^2\mathbf{x}, \tag{44a}$$

$$E_0^2 \tilde{W}_{ij} = \frac{\lambda^2}{2\pi} \iiiint\limits_{\mathbb{R}^2\times\mathbb{R}^2} V_i(\mathbf{x})V_j(\mathbf{x}')K_0(\lambda|\mathbf{x}-\mathbf{x}'|)\, d^2\mathbf{x}\, d^2\mathbf{x}' - \iint\limits_{\mathbb{R}^2} V_i(\mathbf{x})V_j(\mathbf{x})\, d^2\mathbf{x}. \tag{44b}$$

In (44), we have retained E_0^2 as a scaling factor. Note, however, that in (36) (or (35a)) and (39a,b), $\mathbf{E}_0$ is a vector with complex components, representing the polarization of the pump field. This does not scale trivially out of $\boldsymbol{\nabla}\hat{\phi}$, even in the non-self-consistent case (36). Note also that the form (19) is valid only for λ real; for $|\omega| > \boldsymbol{\Omega}_{LH}$ the correct interaction functions must, as in Sec. 4, be obtained by analytic continuation via the upper complex ω half-plane.

Since (19) are still formally valid, we can deduce the same approximate dispersion relations (21) and (28) for the TOD and S–aS instabilities respectively, where $E_0^2 W_{ij}$ and $E_0^2 \tilde{W}_{ij}$ are now defined by (44). It remains to discuss a few points.

(i) *Growth rate of the TOD instability.* It will be proved that the TOD instability can have a positive growth rate for $\omega < -\boldsymbol{\Omega}_{LH}$; i.e. we shall derive a formula to replace (23), showing that $W_{ll}^{(i)} > 0$ for $\omega < -\boldsymbol{\Omega}_{LH}$. To this end, λ is continued as prescribed, obtaining $\lambda = i\chi$, $\chi = (\omega^2 - \boldsymbol{\Omega}_{LH}^2)^{1/2}$ for $\omega < -\boldsymbol{\Omega}_{LH}$. Then, using

$$K_0(iz) = -\tfrac{1}{2}\pi\,[Y_0(z) + iJ_0(z)]$$

Abramowitz and Stegun 1965, we obtain

$$E_0^2 W_{ll}^{(i)} = \frac{\chi^2}{4} \iiiint\limits_{\mathbb{R}^2\times\mathbb{R}^2} V_l(\mathbf{x})V_l^*(\mathbf{x}')J_0(\chi|\mathbf{x}-\mathbf{x}'|)\, d^2\mathbf{x}\, d^2\mathbf{x}'.$$

We then use (Abramowitz and Stegun 1965)

$$J_0(\chi|\mathbf{x}-\mathbf{x}'|) = \frac{1}{2\pi} \int_0^{2\pi} e^{i\mathbf{k}(\theta)\cdot(\mathbf{x}-\mathbf{x}')}\, d\theta,$$

https://doi.org/10.1017/S0022377897005886 Published online by Cambridge University Press

where $\mathbf{k}(\theta) = \chi(\cos\theta, \sin\theta)$. Inserting this and interchanging the order of integration, the formula

$$E_0^2 W_{ll}^{(i)} = \frac{1}{8\pi}\chi^2 \int_0^{2\pi} |\hat{V}_l(\mathbf{k}(\theta))|^2 \, d\theta \tag{45}$$

is obtained, where

$$\hat{V}_l(\mathbf{k}) = \iint_{\mathbb{R}^2} V_l(\mathbf{x}) \exp(i\mathbf{k}\cdot\mathbf{x}) \, d^2\mathbf{x}$$

is the Fourier transform, and $\mathbf{k}(\theta)$ is as defined above. It follows that positive growth rate can be obtained for $\omega < -\mathbf{\Omega}_{LH}$. For $\omega > \mathbf{\Omega}_{LH}$, a similar chain of arguments shows that $W_{ll}^{(i)} < 0$.

(ii) *Symmetry and the S–aS instability.* In the one-dimensional case, it was found that for the symmetric case (i.e. even $N(x)$), the Stokes–antiStokes instability exists only when the participating resonances are either both even or both odd. The corresponding statement for the two-dimensional rotationally symmetric case is that the Stokes–antiStokes instability exists only when the azimuthal mode numbers m and n for the two participating resonances are equal or when they differ by two.

The argument for (ii) is now briefly given. We shall prove that $\tilde{W}_{ij} = 0$ unless the above condition is satisfied. Let the eigenmode $\varphi_i(\mathbf{x})$ have azimuthal mode number m. Then, using the fact that $\mathbf{E}_0 + \boldsymbol{\nabla}\hat{\phi}$ has $m = 1$, we have that $V_i(\mathbf{x})$ has contributions of types $m+1$ as well as $m-1$. Similarly, assuming $\varphi_j(\mathbf{x})$ has azimuthal mode number n, $V_j(x')$ has contributions of types $n+1$ and $n-1$. Considering the integrations (44) in polar coordinates, one can readily see that a non-vanishing contribution can only come from products $V_i(\mathbf{x})V_j(\mathbf{x}')$ that contain terms of the same azimuthal type. Then, the conclusion follows.

8. Application to SEE

In the SEE experiments, the return HF wave is frequency-analysed. The application of the theoretical model discussed in this paper is as follows. The striations, once formed, function as resonators for the incident radio waves. Trapped upper-hybrid oscillations are thereby generated. A spatial average of these upper-hybrid oscillations multiplied by the density fluctuations forms a source current for electromagnetic back-radiation, as discussed in Mjølhus *et al.* (1995). As long as the upper-hybrid response is stable, no sidebands are generated in this way. However, when the thresholds for the parametric instabilities discussed here are exceeded the source current will radiate at sidebands.

Details of this are published elsewhere (Mjølhus and Helmersen 1997). Let us here only point out that the TOD instability predicts a downshift slightly larger than the lower-hybrid frequency. This corresponds to the reported downshifted maximum (DM) (Leyser *et al.* 1994).

The instabilities and the thresholds depend very sensitively on the value of $\mathbf{\Omega}$ and the striation profile $N(\mathbf{x})$. Owing to the good transport along the magnetic field, one may consider $N(\mathbf{x})$ as independent of the position along the magnetic field, while $\mathbf{\Omega} = \mathbf{\Omega}(z)$ (with z the coordinate along $\mathbf{B}_0$) will decrease continuously along the striation, because the background plasma density (i.e. outside the striation) increases. Then,

https://doi.org/10.1017/S0022377897005886 Published online by Cambridge University Press

interpreting (3) (or (32)) as quasiperpendicular, the value of $\Omega(z)$ will be favourable for the TOD instability to the various trapped oscillation resonances, at certain positions z_j along the striation.

One should indeed regard this quasi-one- (two-) dimensional approach as a rather crude approximation. Since the dynamics depend so strongly on $\Omega(z)$, parallel variation of E and n may be strong. However, on breaking this quasiperpendicular model, the resulting model becomes very intractable. It is thought that the perpendicular models discussed in this paper constitute a clean and useful approach to the problem of SEE generation in ionospheric radio modification experiments. In addition to the neglect of parallel variations, the neglect of 'Z-mode leakage' mentioned at the end of Sec. 2 also deserves future consideration.

9. Summary

Simple 'dispersion relations' for parametric instabilities of driven and trapped upper-hybrid oscillations have been obtained. For the trapped oscillation decay (TOD) instability, we have (21), with W_{ll} defined either as in (20) (slab geometry) or as in (44) (two-dimensional striations). In particular, for the imaginary parts, which determine the growth rate and threshold, the beautiful formulae (23) and (45) respectively were obtained for the two cases. Numerical examples of this instability have been shown in Figs 4 and 5.

For the Stokes–antiStokes instability, the dispersion relation obtained is (28). The threshold condition (31) leads to the peculiarities exhibited in Fig. 6(b), namely that

(i) the instability exists below a (negative) value of Ω;

(ii) in this range, it exists for the drive E_0 between an upper and lower value.

The latter feature is seen in the numerical example of Fig. 7, and the former feature is also confirmed in the case considered.

In the numerical examples shown, very regular oscillations developed at the frequencies predicted by the theory. When the drive E_0 is higher than the threshold, a rich variety of dynamical behaviour has been observed, to which we may return in future work.

Acknowledgements

The core of the computer code used to generate Figs 4, 5 and 7 was developed by Erlend Helmersen. The computations were made possible by support from the Research Council of Norway (Programme for Supercomputing) through a grant of computing time. Useful discussions with Dr Per Jakobsen are appreciated.

Appendix A. Numerical model

In the non-stationary numerical results presented, the set of equations that has been solved is

$$\{i(\partial_t + \nu_e) + [\Omega - (n+N) + \partial_x^2]\}E = E_0(n+N) - j_2(t), \tag{A 1a}$$

$$(\partial_t^2 + 2\nu_i^*\partial_t - \partial_x^2 + \Omega_{\mathrm{LH}}^2)n = \partial_x^2|E+E_0|^2, \tag{A 1b}$$

$$j_2(t) = \overline{(n+N)E}. \tag{A 1c}$$

https://doi.org/10.1017/S0022377897005886 Published online by Cambridge University Press

They were solved using periodic boundary conditions. This set differs from (3) by the presence of the term $j_2(t)$, where the bar denotes the spatial average. This vanishes in the infinite interval model (3) discussed in the main text. Moreover, the spatial averages of E, n and N are to vanish. This means that N is chosen as

$$N(x) = -N_0 \exp\left[-\left(\frac{x}{l}\right)^2 \right] - \bar{N}, \tag{A 2a}$$

$$\bar{N} = -\frac{N_0 l \pi^{1/2}}{L}, \tag{A 2b}$$

where L is the system length. In Mjølhus *et al.* (1995), it is argued that this is a natural formalism for separating the electrostatic and electromagnetic components of the oscillating electric field. Then $j_2(t)$ occurs as a source in the equation for the electromagnetic field E_0 on the global spatial scale.

This way of replacing (3) with a finite spatial model requires that care be exercised when one wants to compare the results of the theoretical studies in the main text. For example, the effective value of $\boldsymbol{\Omega}$ will be

$$\bar{\boldsymbol{\Omega}} = \boldsymbol{\Omega} + \bar{N}. \tag{A 3}$$

In all the numerical results shown, we used 4096 Fourier modes, a time step $\delta t = 0.0005$ and a system length $L = 204.8$. The numerical method is further documented in Mjølhus *et al.* (1995).

In the actual numerical runs, a small damping term in the low-frequency equation was used. Otherwise, lower-hybrid waves would have accumulated, propagating around the periodic system.

In all the numerical examples, $N_0 = 55$ and $l = 1.5$ in (A 2). These values were chosen so as to correspond to a density depletion of about 1% and a half-width of about 1–1.5 m in the ionospheric application. The same values were used in the numerical computations behind Figs 3 and 6, but without the mean-value term.

The computations for Figs 1(a) (solid line), 2, 3 and 6 all involve solving (7), or computing eigenfunctions and eigenvalues of L_N. This was done by replacing (7) by finite boundary conditions $\hat{E}(-x_0) = \hat{E}(x_0) = 0$, where $x_0 = al$; $a = 3$ and $a = 5$ were used, giving indistinguishable results. For this finite-boundary-value problem, a finite-difference method described in Keller (1968) was used; this method can easily be shown to work when $N(x) < 0$, provided that $\nu_e \neq 0$. The spatial grid size $\delta x = 0.01$ was used. The eigenfunctions and eigenvalues were also determined using this method: first, the eigenvalues $\boldsymbol{\Omega}_j$ were determined by solving (7a) (with finite boundary conditions) and small ν_e ($\nu_e = 0.1$) and finding the maximum points of $U(\boldsymbol{\Omega})$ (cf. Fig. 2). Then (7a) was solved with $\boldsymbol{\Omega} = \boldsymbol{\Omega}_j$ and with $\nu_e = 0.1$ and $\nu_e = -0.1$; the difference between these two gives an approximation of the eigenfunction, which was then normalized. The odd eigenfunctions were determined similarly, by replacing the right-hand side of (7) with an odd function. The integrals entering W_{ij} and $\tilde{W}_{ij}$ were computed using a simple trapezoidal approximation.

Appendix B. Some properties of W_{ij} and $\tilde{W}_{ij}$

Lemma B. 1. *For λ real, $W_{jj} \leqslant 0$.*

https://doi.org/10.1017/S0022377897005886 Published online by Cambridge University Press

In the proof of this lemma, we shall need Young's inequality

$$||\varphi * f||_p \leqslant ||\varphi||_1 ||f||_p, \tag{B 1}$$

where $*$ means convolution and

$$||f||_p = \left[\int_D |f(x)|^p dx\right]^{1/p}$$

is the L_p norm. A proof of this can be found in Folland (1976).

Proof of Lemma B.1. We shall use $p = 2$. The lemma is true for the one-dimensional case as well as the two-dimensional case. For the region D, we use $\mathbb{R}$ in the one-dimensional case and $\mathbb{R}^2$ in the two-dimensional case. For φ, we have

$$\varphi(x) = \tfrac{1}{2}\lambda e^{-\lambda|x|}$$

in the one-dimensional case and

$$\varphi(\mathbf{x}) = \frac{\lambda^2}{2\pi} K_0(\lambda|\mathbf{x}|)$$

in the two-dimensional case. For both cases, we have

$$||\varphi||_1 \overset{\text{def.}}{=} \int_D |\varphi(x)|\, dz = 1.$$

For the one-dimensional case, this is straightforward, while for the two-dimensional case, a proof is provided below.

For W_{jj}, we can write

$$E_0^2 W_{jj} = \langle V, \varphi * V\rangle - ||V||^2,$$

where $\langle\ ,\ \rangle$ is the standard L_2 inner product

$$\langle F, G\rangle = \int_D FG^*\, dx.$$

One can then use Schwarz' inequality to obtain

$$W_{jj} \leqslant ||V||\ ||\varphi * V|| - ||V||^2.$$

Finally, using (B 1), the assertion follows. □

Lemma B. 2. *$|W_{ij}|^2 \leqslant W_{ii}W_{jj}$ and $|\tilde{W}_{ij}| \leqslant W_{ii}W_{jj}$.*

Proof. W_{ij} and $\tilde{W}_{ij}$ can be expressed as a bilinear form

$$W(U, V) = \langle U, V\rangle - \langle U, \varphi * V\rangle,$$

i.e.

$$E_0^2 W_{ij} = -W(V_i, V_j), \quad \tilde{W}_{ij} = -W(V_i, V_j^*).$$

By Lemma B.1, W is positive ($W(V, V) \geqslant 0$). Consequently, the assertion follows by Schwarz's inequality

$$|W(U, V)|^2 \leqslant W(V, V)W(U, U).$$ □

Lemma B. 3.

$$I(\lambda) = \int_{\mathbb{R}^2} |K_0(\lambda|\mathbf{x}|)|\, d^2\mathbf{x} = \frac{2\pi}{\lambda^2}.$$

https://doi.org/10.1017/S0022377897005886 Published online by Cambridge University Press

Proof. Using the fact that $K_0(r) > 0$, and changing variables $\lambda \mathbf{x} = \mathbf{y}$, and thereafter to polar coordinates, we have

$$I(\lambda) = \frac{2\pi}{\lambda^2} \int_0^\infty r K_0(r)\, dr.$$

Using the differential equation for K_0 Abramowitz and Stegun 1965, we have

$$\int_0^\infty r K_0(r)\, dr = -\lim_{r \to 0} r \frac{dK_0(r)}{dr}.$$

Then the assertion follows from the fact that $K_0(r) \sim -\ln(\frac{1}{2}r)$ as $r \to 0^+$ (Abramowitz and Stegun 1965). □

References

Abramowitz, M. and Stegun, I. 1965 *Handbook of Mathematical Functions*. Dover, New York.

Dysthe, K. B., Mjølhus, E., Pecseli, H. L. and Rypdal, K. 1982 *Physica Scripta* **T2/2**, 548.

Fialer, P. A. 1974 *Radio Sci.* **9**, 923.

Folland, G. B. 1976 *Introduction to Partial Differential Equations*. Princeton University Press.

Friedrichs, K. O. 1948 *Spectral Representation of Linear Operators*. Lecture Notes, New York University.

Gurevich, A. V., Zybin, K. P. and Lukyanov, A. V. 1995 *Phys. Rev. Lett.* **75**, 2622.

Inhester, B. 1982 *J. Atmos. Terr. Phys.* **44**, 1049.

Keller, H. B. 1968 *Numerical Methods for Two-Point Boundary Value Problems*. Blaisdell, Waltham, MA.

Leyser, T. B., Thidé, B., Derblom, H., Hedberg, Å., Lundborg, B., Stubbe, P. and Kopka, H. 1989 *Phys. Rev. Lett.* **63**, 1145.

Leyser, T. B., Thidé, B., Waldenvik, M., Veszelei, E., Frolov, V. L., Grach, S. M. and Komrakov, G. P. 1994 *J. Geophys. Res.* **99**, 19 555.

Mannheimer, W. M. and Ott, E. 1974 *Phys. Fluids* **17**, 1413.

Minkoff, J., Kugelmann, P. and Weissman, I. 1974 *Radio Sci.* **9**, 941.

Mjølhus, E. 1983 *J. Plasma Phys.* **29**, 195.

Mjølhus, E. and Helmersen, E. 1997 *Proceedings of International Workshop on Strong Microwaves in Plasmas* (ed. A. G. Litvak), Vol. 2, pp. 449–467. IAP RAS, Nizhni Novgorod.

Mjølhus, E., Hanssen, A. and DuBois, D. F. 1995 *J. Geophys. Res.* **100**, 17 527.

Rosenbluth, M. N. 1972 *Phys. Rev. Lett.* **29**, 565.

Sanmartin, J. R. 1970 *Phys. Fluids* **13**, 1533.

Stoker, J. J. 1950 *Nonlinear Vibrations in Mechanical and Electrical Systems*. Wiley, New York.

Stubbe, P., Stocker, A. J., Honary, F., Robinson, T. R. and Jones, T. B. 1994 *J. Geophys. Res.* **99**, 6233.

Thidé, B., Kopka, H. and Stubbe, P. 1982 *Phys. Res. Lett.* **49**, 1561.

Waldenvik, M. 1994 The dynamics of electromagnetic radiation from a HF perturbed space plasma. Dr thesis, Uppsala University. (IRF Sci. Rep. 216, Swedish Institute of Space Physics, Uppsala.)

https://doi.org/10.1017/S0022377897005886 Published online by Cambridge University Press